




# Impulse Response Characterization of a Commercial Multimode Fiber Using Superconducting Nanowire Single-Photon Detectors

Yuanhang Zhang , Nicolas K. Fontaine , Senior Member, IEEE, Mikael Mazur , Member, IEEE, Haoshuo Chen , Member, IEEE, Roland Ryf , Fellow, IEEE, Guifang Li , Fellow, IEEE, and Andrea Blanco-Redondo

**Abstract**—Time-of-flight measurements are key to study distributed mode coupling and differential mode group delay (DMDG) in multimode fibers (MMFs). However, current approaches using regular photodetectors with limited sensitivity preclude the detection of weak modal interactions in such fibers masking interesting physical effects. Here we demonstrate the use of high-sensitivity superconducting nanowire single-photon detectors (SNSPDs) to measure the mode transfer matrix of a commercial graded-index multimode fiber. Two high performance 45-mode multi-plane light conversion (MPLC) devices served as the mode multiplexer/demultiplexer. Distributed mode coupling and DMDG among different mode groups are accurately quantified from the impulse response measurement. We also observed cladding modes of the MMF as a pedestal of the pulse in the measurement. This work paves the way for applications such as quantum communications using many spatial modes of the fiber.

**Index Terms**—Multi-plane light conversion (MPLC), transfer matrix, differential mode group delay (DMGD), distributed mode coupling, impulse response, superconducting nanowire single-photon detector (SNSPD).

## I. INTRODUCTION

MODE-DIVISION multiplexing (MDM) in multimode fibers (MMFs) as a candidate for next generation high-capacity optical transmission systems, has attracted great research interest in the last decade [1], [2]. The mode dynamics in

Manuscript received 30 November 2021; revised 1 April 2022 and 29 April 2022; accepted 30 April 2022. Date of publication 17 May 2022; date of current version 2 August 2022. The work of Y. Zhang was supported by the China Scholarship Council (CSC) Scholarship No. 201606250006. This work was supported in part by NSF under Grant ECCS-1932858, in part by ARO under Grants W911NF1710553 and W911NF2010085, and in part by ARL under Grant W911NF1920265. (Corresponding author: Andrea Blanco-Redondo.)

Yuanhang Zhang is with the Nokia Bell Labs, New Providence, NJ 07974 USA, and also with CREOL, College of Optics and Photonics, University of Central Florida, Orlando, FL 32816 USA (e-mail: yuanhangzhang@knights.ucf.edu).

Nicolas K. Fontaine, Mikael Mazur, Haoshuo Chen, Roland Ryf, and Andrea Blanco-Redondo are with Nokia Bell Labs, New Providence, NJ 07974 USA (e-mail: nicolas.fontaine@nokia-bell-labs.com; mikael.mazur@nokia-bell-labs.com; haoshuo.chen@nokia-bell-labs.com; roland.ryf@nokia.com; andrea.blanco-redondo@nokia-bell-labs.com).

Guifang Li is with CREOL, College of Optics and Photonics, University of Central Florida, Orlando, FL 32816 USA (e-mail: li@creol.ucf.edu).

This article has supplementary material provided by the authors and color versions of one or more figures available at <https://doi.org/10.1109/JLT.2022.3172239>.

Digital Object Identifier 10.1109/JLT.2022.3172239

MMFs are complex: spatial modes in these fibers couple with each other due to perturbations from the environment, imperfect geometry or refractive index fluctuations, and optical pulses propagating in MMFs suffer from modal dispersion, with each mode traveling at a different group velocity. The arrival time difference of two modes in a fiber is defined as differential mode group delay (DMGD) and it has been extensively studied in optical communications as it directly determines the number of equalizer taps necessary to compensate for the mode coupling [3]. Measuring the intensity impulse response is an important method to study DMGD and mode coupling.

Current methods to measure the impulse response of MMFs — including time-of-flight techniques [4], [5], swept-wavelength interferometry (SWI) [6], optical time-domain reflectometry (OTDR) [7], and digital signal processing (DSP) [8] — fail to measure long fiber spans and very weak inter-modal interactions due to the limited sensitivity of regular photodetectors. The capability of detecting light at the single-photon level has enabled breakthroughs in many fields, such as reconfigurable photonics [9], light detection and ranging (LiDAR) [10], and optical quantum information applications [11] including quantum computing [12], [13] and quantum key distribution [14]. Recently, using ultrasensitive single-photon detectors to study fiber modes has attracted some attention. In 2019, Johnson *et al.* measured the temporal evolution of orbital angular momentum (OAM) modes at telecommunication wavelengths using a single-pixel camera with a single-photon avalanche diode (SPAD) detector and a digital micro-mirror device (DMD) [15]. In 2020, Chandrasekharan *et al.* measured the group velocity dispersion, the DMGD, and the effective refractive index difference of different spatial modes in a 6-mode fiber using a two-dimensional (2D) SPAD array, over a broad bandwidth (500 nm–610 nm) in the visible regime [16]. However, 2D SPAD arrays are not available at telecommunication wavelengths because of the high cost of fabricating pixelated arrays. Further superconducting nanowire single-photon detectors (SNSPDs) show significantly better performance at these wavelengths. At 1550 nm, commercially available SPADs have a timing jitter of ~150 ps, quantum efficiencies of ~20–30 %, and dark count rates of ~50 Hz [17]. In contrast, the commercial SNSPD (Single Quantum Eos) in our group has a timing jitter of ~10 ps, a quantum efficiency of ~85%, and dark count rates of >10 Hz. Notably, SNSPDs with sub-3 ps temporal

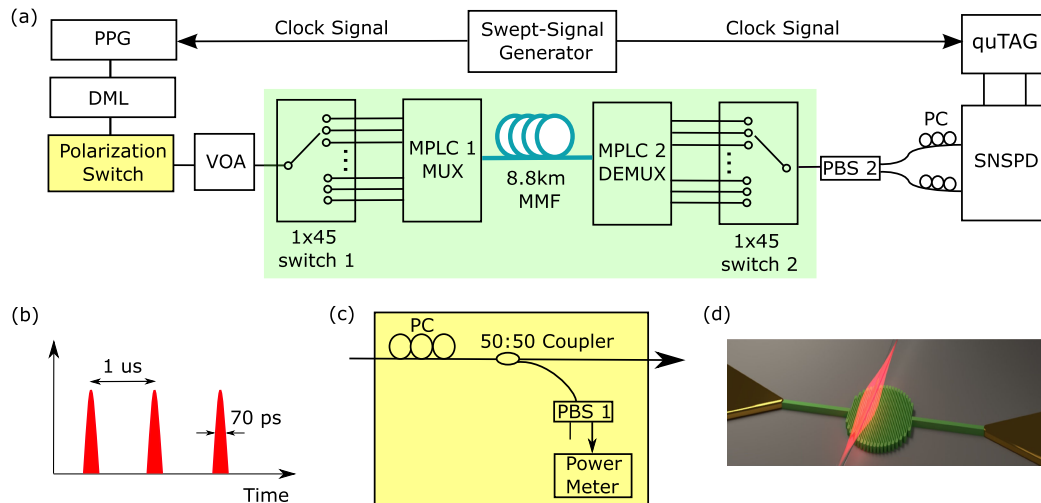


Fig. 1. (a) Experimental setup for the transfer matrix measurement. PPG: pulse pattern generator; DML: directly modulated laser; VOA: variable optical attenuator; MPLC: multi-plane light converter; MUX/DEMUX: multiplexer/demultiplexer; PBS: polarization beam splitter; PC: polarization controller; SNSPD: superconducting nanowire single-photon detector. (b) Output periodic pulses of the DML. (c) Components used to make the polarization switch. (d) Artist impression of a SNSPD, with photons (red color) impinging on a superconducting meandering nanowire (green color). The detector transits from superconducting state to a resistive state upon absorption of a single photon. As a result, a voltage pulse is created, and a detection event is registered (Courtesy of Single Quantum) [20].

resolution have been demonstrated [18]. In 2021, Mazur *et al.* did a proof-of-principle impulse response measurement of a few-mode fiber using the SNSPD and a 3-mode photonic lantern as the mode demultiplexer [19]. In this paper, we measure the impulse response of the dual-polarization  $45 \times 45$  transfer matrix of a commercial OM3 multimode fiber. With the high sensitivity of SNSPDs, we build the histogram of the impulse response at a single-photon level, enabling us to study very weak modal interactions. The very low dark count rate used ( $\sim 200$  Hz) determines a noise floor of  $-136$  dBm, giving us the capability to observe the distributed mode crosstalk and the cladding modes directly at the foot of the pulse. Using the high timing accuracy of  $\sim 10$  ps, the DMGD can be accurately measured. Two high performance 45-mode multiplexer/demultiplexer based on the multi-plane light conversion (MPLC) technology and two optical MEMS (micro-electromechanical system) switches are used to excite and receive one specific spatial mode of the MMF at every single step.

This paper is structured into five sections. Section II describes the experimental setup and some critical components used in the measurement. Section III analyzes the results of two cases: the back-to-back (BTB) transmission and transmission with the MMF inserted. DMDG and distributed crosstalk plateau among different mode groups are accurately quantified. Section IV discusses a 3-mode coupling model to shed light on the measured results. Finally, Section V concludes the paper.

## II. EXPERIMENTAL SETUP

The experimental setup is outlined in Fig. 1. A swept-signal generator (Agilent 83650B) provided a sinusoidal clock signal (8000 MHz, 125 ps) for the pulse pattern generator (PPG, Anritsu MP1763B). The PPG divided the clock signal by 8000 (1 MHz, 1  $\mu$ s) and generated square pulses to drive a directly modulated laser (DML). This DML is a distributed feedback

(DFB) laser with a measured wavelength of 1545 nm. The swept-signal generator also provided an external clock signal for the quTAG (qutools company) for synchronization. The quTAG is a fast time-to-digital converter and time tagging device for time correlated single-photon counting (TCSPC). The DML has a pulse repetition rate of 1 MHz, and each pulse has a measured full width at half maximum (FWHM) of 70 ps. We chose a repetition rate of 1 MHz as the detectors have peak efficiency ( $\sim 85\%$ ) at this rate, while higher rates are measurable at the expense of lower detection efficiency. The average output power of the DML was measured to be  $-36.0$  dBm. To fully characterize the dual-polarization  $45 \times 45$  transfer matrix, a manually controlled polarization switch, shown in Fig. 1(c), was used in front of the mode multiplexer, and a fiber-based polarization beam splitter (PBS) was used after the mode demultiplexer to realize a polarization-diverse measurement. The polarization switch, as shown in Fig. 1(c), consists of a polarization controller (PC), a 50:50 fiber coupler, a fiber-based PBS (Thorlabs, PBC1550SM-APC) and a power meter (HP 8153 A). A pair of optical switches (DiCon MEMS 64-channel model) and MPLCs constitute the function of mode-diverse measurement (green background in Fig. 1(a)). Outputs from the second PBS were connected to two independent channels of the SNSPD system. Since the meandering nanowire inside the SNSPD is polarization sensitive, two PCs were added between the second PBS and the SNSPD. Any path length mismatch (either in fiber or RF cable) induced a relative time shift for pulses in different channels, which was corrected during the post-processing of data.

To launch the  $x$ -polarization state into the system with the polarization switch shown in Fig. 1(c), we first adjusted the PC manually until reading the maximum power ( $-39.6$  dBm) on the power meter. Then we scanned all 45 channels of switch 1 and switch 2 sequentially, with the received  $x$ - and  $y$ -polarization states recorded simultaneously under  $x$ -polarization launch. Following, we adjusted the PC until reading the minimum power

(−70.0 dBm), to launch  $y$ -polarization state and repeated the above mode-diverse measurement. In this way, we make sure  $x$ - and  $y$ - polarization launch states are orthogonal. Those two optical switches and the quTAG were controlled by one single computer to record data. For every cell of the  $45 \times 45$  matrix, 30 s of raw data was saved to accumulate enough data points to plot the histogram. Measuring a complete dual-polarization transfer matrix needed roughly 34 hours. We measured the  $45 \times 45$  transfer matrix in a back-to-back (BTB) experiment first (splicing the pigtail fibers of two MPLCs directly [21]). After taking data of the entire transfer matrix of the BTB, we inserted a spool of commercial MMF and repeated the measurement. The VOA helped to attenuate the light to the single-photon level. It had an attenuation of 33 dB for the BTB measurement and was adjusted to 30 dB after inserting the MMF. In this way, the SNSPD reads a similar photon count rate for BTB and MMF measurement. Note that without introducing a 30 dB loss via the VOA, we can measure  $\sim 100$  km long MMFs [19].

In the BTB when both switches were switched to channel 1 ( $HG_{00}$  mode to  $HG_{00}$  mode coupling), the total power reaching the SNSPD was estimated to be −95 dBm. Since such a low power cannot be measured directly with a normal photo detector, we set the VOA to 0 dB attenuation first, and measured the power before the second PBS being −62 dBm. The total insertion loss of these two switches and MPLCs was measured to be 18 dB. Other losses in the link are from the 50:50 fiber coupler, connectors, and some single mode fiber (SMF) connecting components between two labs.

The SNSPD was cooled down by helium to 2.6 K and the bias current of each individual detector was set just below the critical current of the nanowires, leading to a dark count rate of about 200 counts/s, corresponding to a sensitivity of −136 dBm. The detector would transit from a superconducting state to a resistive state upon absorption of a single photon. In our experiment, all lights in the lab were turned off when calibrating the dark count rate, and most of the setup including the MMF fiber spool and MPLCs were covered with aluminum foil to reduce the influence from surrounding light. Covering the setup is important to reach a low dark count rate because background light may couple into the fiber due to blackbody radiation at room temperature [22].

This SNSPD system has 4 independent channels, of which channel 3 and channel 4 were used in the experiment to register the received light with  $x$  and  $y$  polarizations separately. At 1550 nm, channel 3 and 4 have a system detection efficiency of 81% and 85%, respectively. The calibrated timing jitter of channels 3 and 4 are 19.0 ps and 13.2 ps FWHM, respectively. The measured relaxation time (full recovery time after each detection event) is about 100 ns, limiting the maximum count rate to roughly 10 MHz. The detection speed therefore, is much lower than the regular balanced photodetectors (BPDs) commonly used in coherent optical communications, which can have a bandwidth up to 100 GHz. The quTAG has a measured single channel timing jitter of 5.94 ps RMS and 14.00 ps FWHM.

A spool of commercially available OM3 graded-index multimode fiber (GI-MMF, OFS LaserWave FLEX 300) was measured in the experiment. The fiber has a total length of 8851 m, and it was believed to support 9 mode groups (45 spatial modes)

TABLE I  
45 HG MODES SUPPORTED BY THE MPLC

Group 1	$HG_{00}$
Group 2	$HG_{01} HG_{10}$
Group 3	$HG_{02} HG_{11} HG_{20}$
Group 4	$HG_{03} HG_{12} HG_{21} HG_{30}$
Group 5	$HG_{04} HG_{13} HG_{22} HG_{31} HG_{40}$
Group 6	$HG_{05} HG_{14} HG_{23} HG_{32} HG_{41} HG_{50}$
Group 7	$HG_{06} HG_{15} HG_{24} HG_{33} HG_{42} HG_{51} HG_{60}$
Group 8	$HG_{07} HG_{16} HG_{25} HG_{34} HG_{43} HG_{52} HG_{61} HG_{70}$
Group 9	$HG_{08} HG_{17} HG_{26} HG_{35} HG_{44} HG_{53} HG_{62} HG_{71} HG_{80}$

at 1550 nm. In this experiment however, we found it supports 10 mode groups (55 spatial modes), and the last two mode groups behave differently from the first 8 mode groups, as shown in Fig. 7(b). The same fiber has been used in a mode-division multiplexed transmission experiment in 2014 by Ryf *et al.* [23]. According to [23], this OM3 MMF has a measured attenuation loss of 0.34 dB/km for the  $LP_{01}$  and  $LP_{11}$  modes at 1550 nm, and a chromatic dispersion parameter of  $\sim 20$ – $24$  ps/nm/km. However, accurate measurements of the distributed crosstalk, the DMGD, and the cladding modes of this kind of fiber remained elusive, as they were beyond the sensitivity and temporal resolution of previously used detectors.

We use two MPLCs as the mode multiplexer/demultiplexer. The 45-mode MPLC is a free space device consisting of a collimated linear SMF array, a phase mask plane, a dielectric mirror, and a collimated GI-MMF at the output, as shown in Fig. 2(a). The device maps every input Gaussian spot from the SMF array into a specific Hermite-Gaussian (HG) mode through a unitary transformation [21], [24]. As a reciprocal device, this device can be used either as a mode multiplexer (input through SMF end) or a mode demultiplexer (input through GI-MMF end). The performance of the two MPLCs are qualitatively shown by imaging the free space output modes using an InGaAs camera, as shown in Fig. 2(b) and (c). The HG modes in Fig. 2(c) are not as clear as those in Fig. 2(b), indicating the 2nd MPLC that used as the mode demultiplexer has a compromised performance compared to the first one. This was due to an imperfect packaging after assembling, leading to a relatively large insertion loss (IL) and mode dependent loss (MDL). 45 HG modes are grouped into 9 mode groups, and labeled in an order as shown in Table 1. Modes within the same group are degenerate (having nearly equal propagation constant, and thus similar phase velocity and group velocity) and tend to couple strongly during propagation in a fiber. Actually, the 3-m pigtail fibers at the output end of two MPLCs are already long enough to induce mode coupling within the same mode group [21].

### III. EXPERIMENTAL RESULTS

30 s of time-of-flight measurement data were saved per polarization per mode of the  $45 \times 45$  transfer matrix. The data was used to build a histogram covering  $1 \mu\text{s}$ , i.e., the pulse period of the DML. A zoom-in time window around the pulse of the entire  $45 \times 45$  matrix are plotted in the **supplementary figure 1** for BTB and **supplementary figure 2** for MMF. Fig. 3 shows

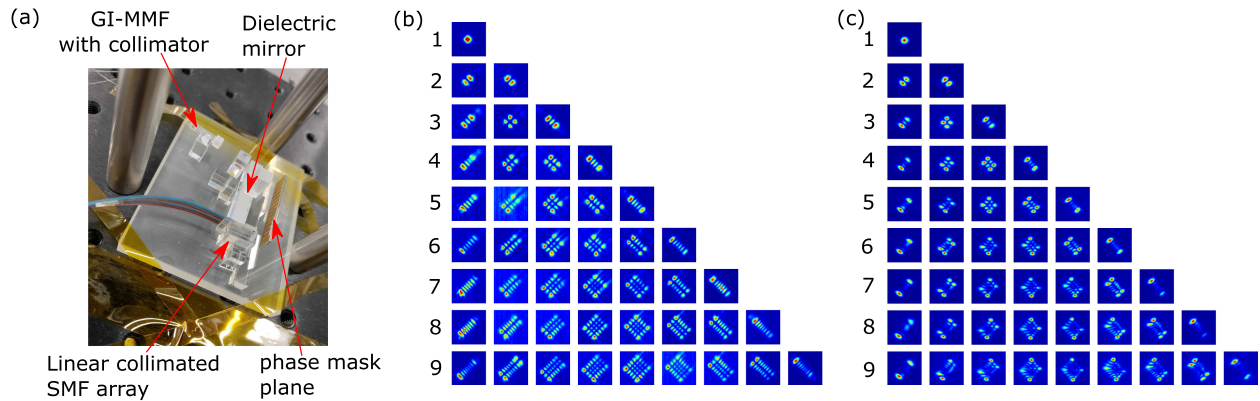


Fig. 2. (a) Photograph of one of the 45-mode MPLC devices used in the experiment. The multi-mode output end of this device has a 3-m long GI-MMF with a collimator. Free-space output modes of (b) MPLC 1 and (c) MPLC 2 captured by an InGaAs camera. Modes of 2nd MPLC are not as clear as the 1st MPLC due to imperfect packaging. 45 Hermite-Gaussian modes are grouped into 9 mode groups. Modes within the same group are degenerate and tend to couple strongly during propagation in a fiber.

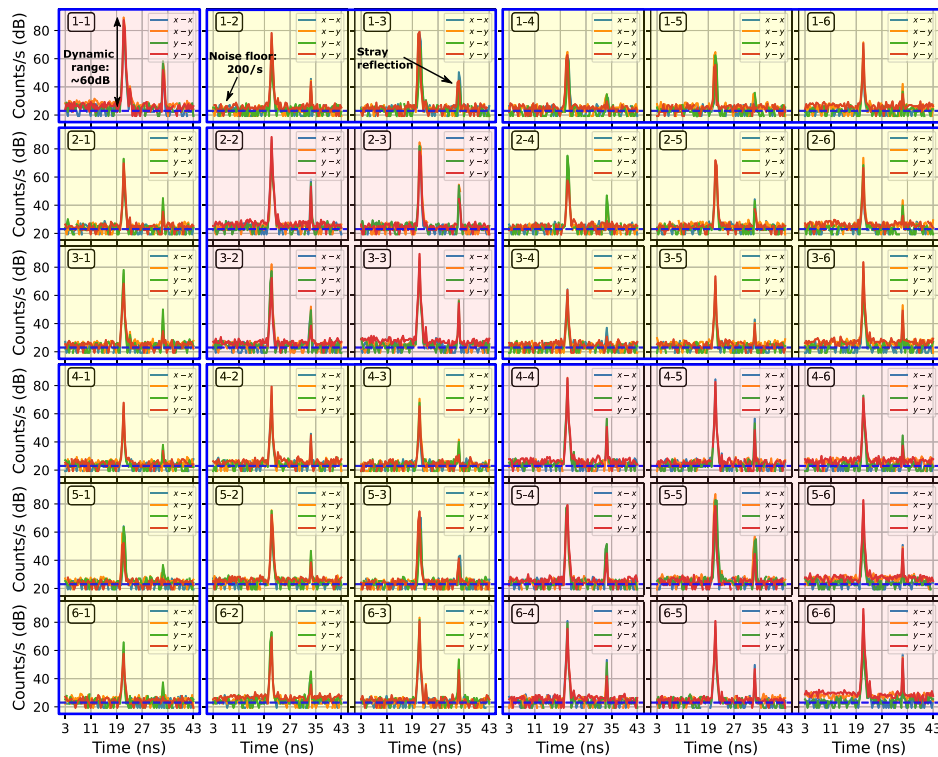


Fig. 3. Histograms of photon arrival time of the BTB experiment. This figure shows the  $6 \times 6$  matrix of the up-left corner of the entire  $45 \times 45$  transfer matrix, with all polarizations presented in one subplot. Readers interested in the complete  $45 \times 45$  matrix can find it in the **supplementary figure 1**. The number (format 'A-B') in the round box in each subplot denotes the coupling from mode A to mode B. The blue dash line indicates the dark count rate of 200 counts/s (noise floor). Cells with the pink background color represent mode coupling of the same mode group while yellow color represent mode coupling among different mode groups.

the histograms of the  $6 \times 6$  matrix of the up-left corner of the entire  $45 \times 45$  transfer matrix of the BTB measurement, with all polarizations presented in one subplot. The peak that appears at about 21 ns is the received pulse from the DML, while the peak at about 33 ns is stray reflection. Without a noticeable pedestal at the foot of the pulse, the dynamic range is as large as 60 dB. These subplots are grouped into different blocks, with cells of the pink background color represent mode coupling of the same mode group and yellow color represent mode coupling among different mode groups.

Similar to Fig. 3, Fig. 4 shows the histograms of the  $6 \times 6$  matrix on the up-left corner of the entire  $45 \times 45$  transfer matrix with the MMF inserted. Distributed mode coupling and DMGD can be observed between 691 and 705 ns. Modes within the same group (e.g.,  $HG_{01}$  and  $HG_{10}$ ) arrive at the same time due to degeneracy and thus have overlapped peaks in time. The crosstalk plateau between individual mode peaks is a clear sign of mode mixing. The plateau between the peaks is due to photons that experienced coupling from one mode to another mode somewhere along the fiber during propagation,

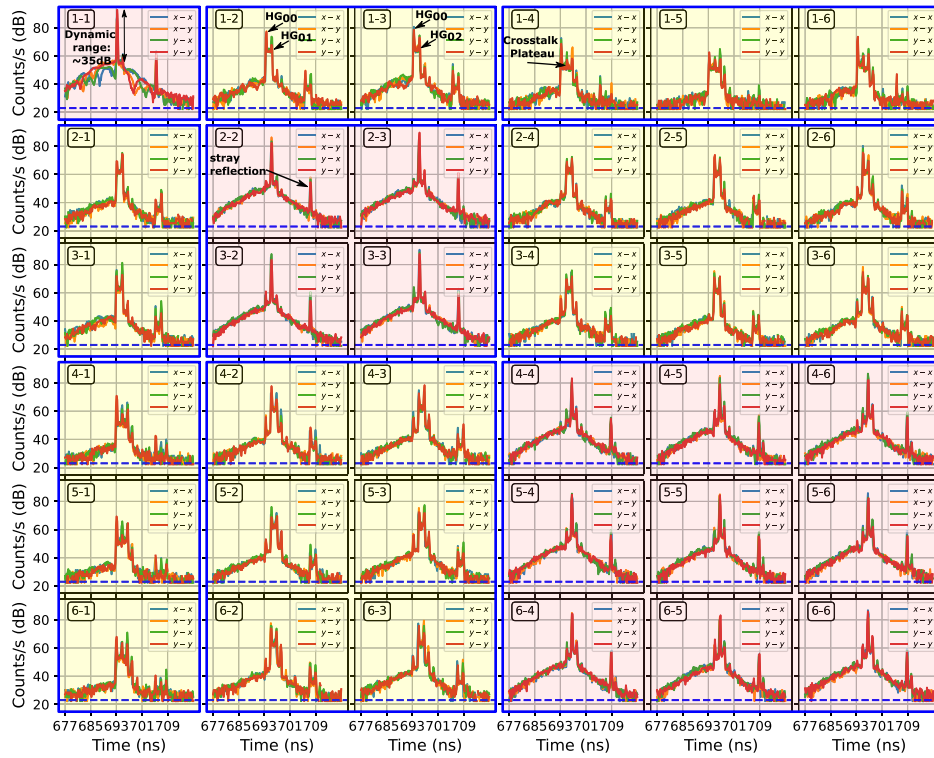


Fig. 4. Histograms of photon arrival time with the MMF inserted. This figure shows the  $6 \times 6$  matrix of the up-left corner of the entire  $45 \times 45$  transfer matrix, with all polarizations presented in one subplot. Readers interested in the complete  $45 \times 45$  matrix can find it in the **supplementary figure 2**. The number (format ‘A-B’) in the round box in each subplot denotes the coupling from mode A to mode B. The blue dash line indicates the dark count rate of 200 counts/s (noise floor). Cells with the pink background color represent mode coupling of the same mode group while yellow color represent mode coupling among different mode groups.

with an arrival time between that of the photons that did not experience mode coupling. Same as Fig. 3, we use pink and yellow background color to represent mode coupling of the same mode group and among different mode groups, respectively. In Fig. 5, all polarizations and mode coupling curves within the same colored block in Fig. 4 are grouped in one subplot, with a zoom-in view. In this way we group the original  $45 \times 45$  matrix into a  $9 \times 9$  matrix, considering degeneracy of modes in the same group. Fig. 6 shows some selected cells with an enlarged view. In measurements with the MMF, the dynamic range is about 35~45 dB, limited by a pedestal at the foot of the pulse. As shown in Figs. 4 and 6, the value of the pedestal changes for different elements in the  $45 \times 45$  matrix. The general trend is that diagonal elements, which have larger count rates, also possess a higher pedestal level, such as in Fig. 6(a) and (b). Some off-diagonal elements, e.g., Fig. 6(c) and (d), the pedestal is below the noise floor determined by the dark count rate (~200 counts/s, -136 dBm). Histograms of the BTB data in Fig. 3 lack the pedestal, indicating that the pedestal is not due to the limited extinction ratio of the DML [19], but most likely to the cladding modes of the MMF. This bend optimized OM3 MMF has a trench at the refractive index profile of core-cladding interface (see Fig. 1(a) in [23]). Cladding modes could be guided between the trench and plastic coating, which have a lower refractive index than the cladding. The silica cladding of the fiber can support hundreds of cladding modes and bending or other environment perturbations may violate the total internal reflection condition and cause mode energy to leave the core mode and couple to

cladding modes [25]. The coupling back-and-forth between core modes and cladding modes during propagation and coupling among different coils of the fiber spool are responsible for the presence of cladding mode. For some cells (e.g. 41-41 in Fig. 6(b)) at the bottom-right corner of the  $45 \times 45$  MMF matrix (see **supplementary figure 2**), a “bump” appears at about 690 ns, 3 ns to the left of mode group 1. Further measurements confirm the “bump” is actually energy coupled to mode group 10, as discussed below in Fig. 7(b).

Fig. 7(a) plots all  $45 \times 45$  cells of the MMF measurement together, with all curves well aligned in time. However, only 8 mode group peaks, instead of 9, are distinguishable in the plot. Note the 8 small peaks following the 8 main peaks are due to stray reflection in the system, as discussed in the supplementary part. To investigate the reason we measured the same MMF with a swept-wavelength interferometer (SWI) from 1450 nm to 1650 nm [26], shown as a spectrogram in Fig. 7(b). 10 bright lines represent 10 mode groups supported by the MMF in this wavelength range. The blue dash line at 1545 nm is the wavelength used in the SNSPD measurement. Clearly, mode group 9 (G9) lies in the crosstalk plateau between G6 and G7 at 1545 nm. This explains why only 8 mode groups peaks appear in Fig. 7(a). And note that mode group 10 (G10) arises as a “bump” about 3 ns to the left of mode group 1 (G1). The cut-off frequency of G10 is about 1555 nm. Lines corresponding to higher order mode groups are broader than lower order mode groups due to the existence of more vector modes with slightly different propagation constants in those mode groups [26]. The slope of the lines

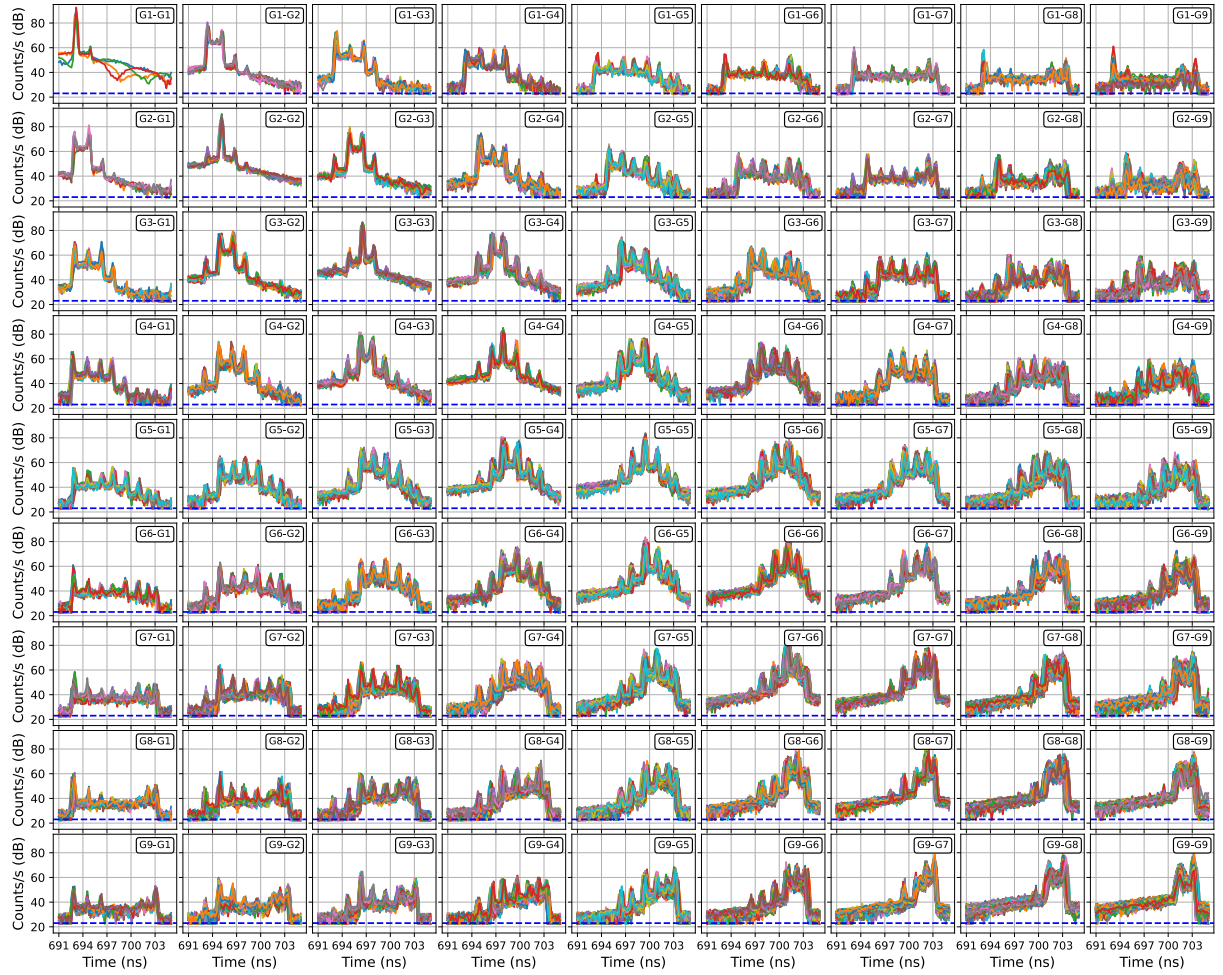


Fig. 5. Histograms of mode group coupling. The entire  $45 \times 45$  matrix is grouped into a  $9 \times 9$  matrix. All polarizations and coupling pulses belong to the same mode group are plotted in one subplot. The blue dash line indicates the dark count rate of 200 counts/s (noise floor).

shows chromatic dispersion, with modes in G9 and G10 having opposite dispersion sign than those in groups G1 to G8 because they are less confined in the fiber core. In Fig. 7(c) we plot cross sections of Fig. 7(b) at 1500 nm, 1545 nm, and 1600 nm. Even though the SWI setup uses coherent detection, pedestal is not observed due to the limited sensitivity of regular balanced photodetectors. Fig. 7(d) gives the diagram of the SWI setup. We use a Faraday mirror in the reference arm to compensate polarization modal dispersion. Simple off-axis launch and collection from the SMF was used for the 8.85 km MMF to observe all modes groups.

The DMGD values can be easily read out from the impulse response graph in Fig. 7(a) or the spectrogram in Fig. 7(b). The relative delay of G2, G3, G4, G5, G6, G7 and G8 to G1 are 1.97 ns, 3.35 ns, 4.73 ns, 6.31 ns, 7.88 ns, 9.07 ns and 10.06 ns, respectively, close to the DMGD numbers reported in a previous publication using the same fiber [23].

Mode coupling can occur both in the transmission fibers or in the mode (de)multiplexers. The distributed mode coupling, however, reflects the coupling properties of the MMF. To study the distributed coupling strength in the commercial MMF, we

analyze the mode crosstalk plateau between peaks in Fig. 5. The plateau values in counts/s, averaged over all polarizations and degenerate modes within each cell for the first 8 mode groups, are shown in Fig. 8(b), and the normalized distributed crosstalk coefficients are shown in Fig. 8(c). Details of this normalization are described below, which is similar to the integral calculation method in [27].

Fig. 8(a) schematically shows an impulse response histogram with multiple mode peaks and the distributed crosstalk plateau in between. The  $y$ -axis of the histogram has a unit of counts/s, corresponding to optical power. Thus the integral over time gives total photon counts, corresponding to the total energy of a specific time window. The red box in Fig. 8(a) indicates the integral area for energy in the crosstalk plateau  $E_{\text{plateau}}$ . DMGD values measured from Fig. 7 are used to determine the start and end time of the plateau when calculating the integral area. If we denote the  $x$ - $x$  polarization curve in cell  $(i, j)$  of the original  $45 \times 45$  matrix as  $P_{ij,xx}(t)$ , the total energy of the curve is given by

$$E_{ij,xx} = \int_{t_1}^{t_2} P_{ij,xx}(t) dt \quad (1)$$

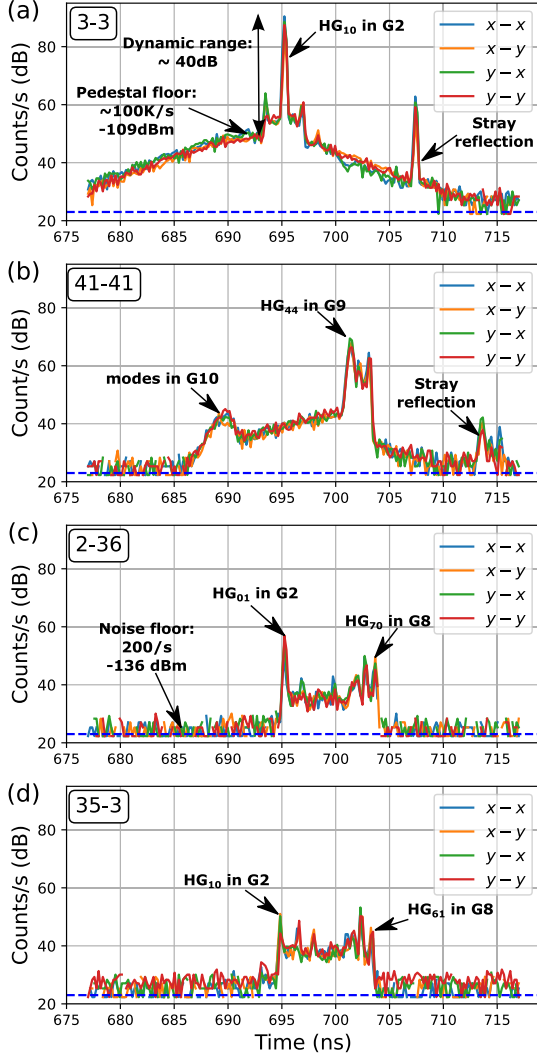


Fig. 6. Selected elements from the entire  $45 \times 45$  transfer matrix with the MMF inserted: (a) 3-3 coupling, (b) 41-41 coupling, (c) 2-36 coupling, and (d) 35-3 coupling. For some elements, e.g. the 2-36 at the off-diagonal region of the  $45 \times 45$  matrix, the pedestal is not obvious as in other elements. The blue dash line indicates the dark count rate of 200 counts/s.

with  $i = 1, 2, \dots, 45, j = 1, 2, \dots, 45$ .  $t_1$  and  $t_2$  are the start and end time of the selected time window, respectively. Then we average over all four polarization curves in each cell, and sum up all columns in each row of the matrix to get pulse energy of each input channel with a specific received polarization state. Finally, we average the pulse energy of 45 input channels and use that number to normalize the distributed crosstalk plateau.

$$\bar{E}_{\text{pulse}} = \frac{1}{45} \sum_{i=1}^{45} \sum_{j=1}^{45} \frac{E_{ij,xx} + E_{ij,xy} + E_{ij,yx} + E_{ij,yy}}{4} \quad (2)$$

$$\bar{E}_{\text{plateau}}(\text{dB/km}) = 10 \times \log_{10} \left( \frac{E_{\text{plateau}}/\bar{E}_{\text{pulse}}}{L} \right) \quad (3)$$

where  $L$  is the length of fiber in km. We use  $t_1 = 677$  ns and  $t_2 = 717$  ns, as shown in Fig. 6, which encompasses all relevant counts resulting from the pulse. The normalized distributed crosstalk coefficients are shown in Fig. 8(c). The

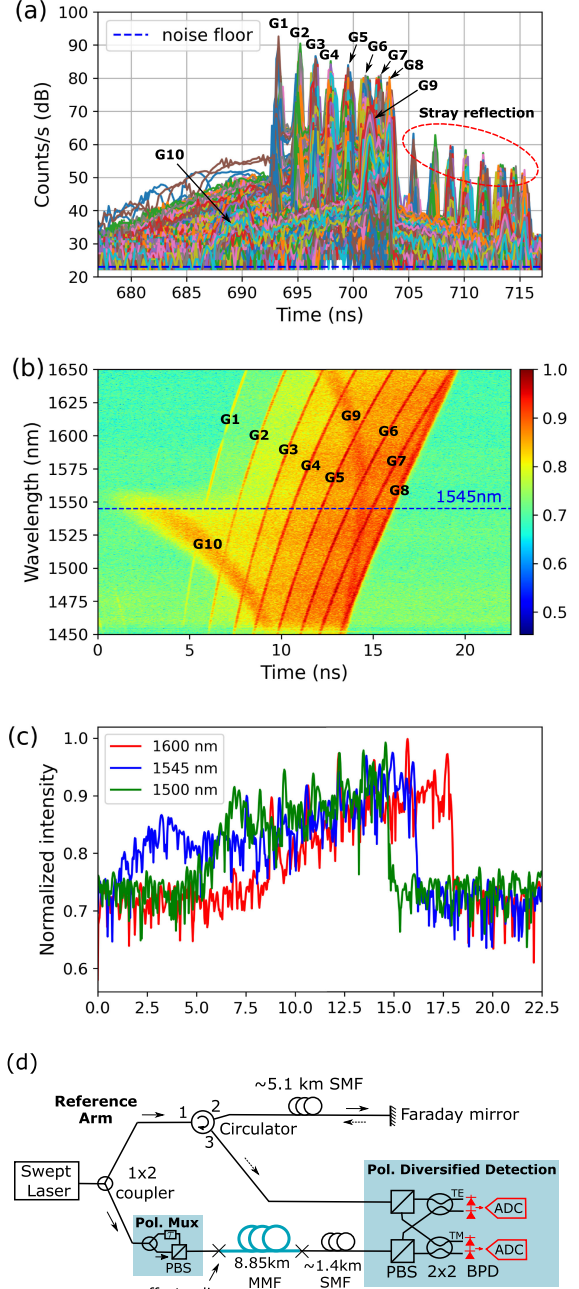


Fig. 7. (a) Plotting all curves of the  $45 \times 45$  cells of the SNSPD data in one subplot. Only 8 mode group peaks are clearly distinguished. (b) Spectrogram of the same MMF measured using a swept-wavelength interferometer. The blue dash line indicates the laser wavelength (1545 nm) used in the SNSPD measurement. Intensity has been normalized. (c) Cross lines of (b) at 1500, 1545, and 1600 nm. (d) Setup of the swept-wavelength interferometer. BPD: balanced photodetectors. Faraday mirror was used to compensate polarization modal dispersion.

diagonal structure of Fig. 8(b) and (c) indicates that adjacent mode groups tend to couple more strongly than groups that are far away.

The complete  $45 \times 45$  mode transfer matrix of BTB and MMF, averaged over all polarizations, are shown in Fig. 9(a) and (b) respectively. For Fig. 9(a), photon count rates between 16 ns and 30 ns are integrated using (1), while for Fig. 9(b),

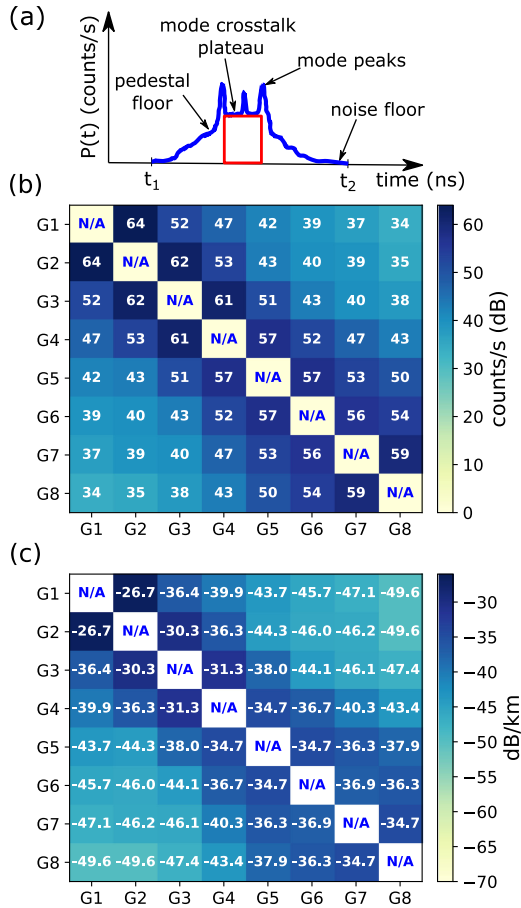


Fig. 8. Coupling strength of distributed crosstalk plateau. (a) Schematic of the impulse response histogram used for normalization. The red box represents the integration area for total counts in the crosstalk plateau. (b) Distributed crosstalk plateau values averaged over all polarizations and all degenerate modes in every cell of Fig. 5 for the first 8 mode groups. (c) Distributed crosstalk plateau coefficients normalized to pulse energy and fiber length.

photon count rates between 691 ns and 705 ns are integrated. The result of counts summation in this 14 ns time window represents the energy transfer matrix of the entire system, giving mode coupling information of both the MPLC mode (de)multiplexer and the MMF. Fig. 9(b) is smoother than Fig. 9(a) due to the mode mixing and modal dispersion in the 8.85 km MMF. Note that the mode mixing in Fig. 9(a) is partly due to the short pigtail fiber at the output of each MPLC, and partly due to the imperfection of the packaged MPLC mode demultiplexer, as shown in Fig. 2(c).

#### IV. DISCUSSION

In this section, we use a simplified 3-mode coupling model to explain the mode coupling process, as shown in Fig. 10. There is a pair of 3-mode multiplexer (MUX) and demultiplexer (DEMUX) connected to a 3-mode fiber. The mode MUX has energy coupling efficiencies of  $\alpha_{ij}$ , representing energy coupling ratio from port  $i$  to mode  $j$ . The mode DEMUX has energy coupling efficiencies of  $\beta_{ij}$ , representing coupling ratio from mode  $i$  to port  $j$ . Mode coupling in the 3-mode fiber is described by a matrix  $\gamma$  with element  $\gamma_{ij}$  representing energy coupling ratio from mode  $i$  to mode  $j$ .

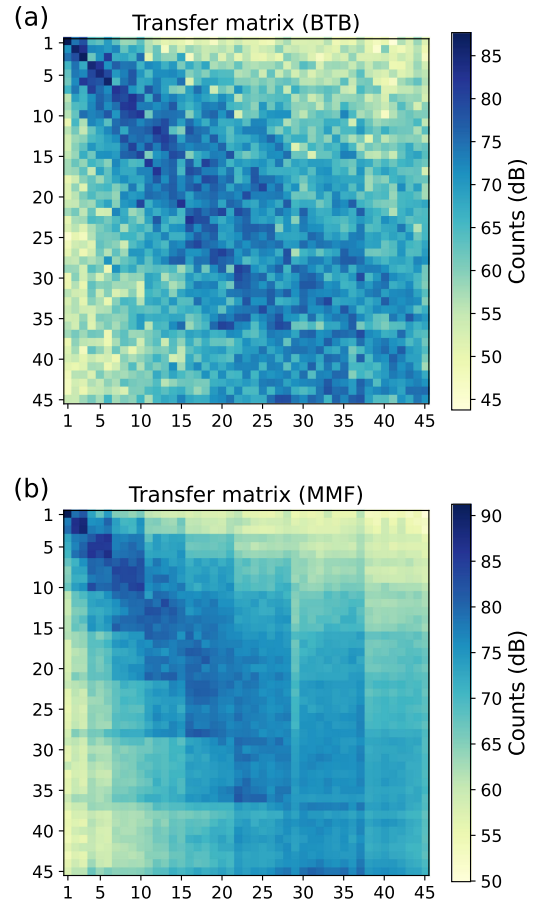


Fig. 9. The complete  $45 \times 45$  mode transfer matrix, averaged over all polarizations of (a) BTB and (b) MMF, shows the coupling among all modes. (b) is smoother than (a) due to the mode mixing and modal dispersion in the 8.85 km MMF. Note that (a) and (b) are plotted using different colormap ranges intentionally because BTB and MMF have slightly different photon count rates (input powers).

Before launching into the full description, we would like to emphasize a few points:

- This 3-mode fiber supports three modes/mode groups G1, G2, G3 with distinguishable group velocities  $v_1 > v_2 > v_3$ . They are labeled by red, green and blue color respectively in Fig. 10 to be easily recognizable. At the end of fiber, mode peaks of G1, G2, G3 appear at  $t_1$ ,  $t_2$ , and  $t_3$  in the impulse response plot, respectively.
- Matrix  $\alpha$  and  $\beta$  are not necessarily symmetric, but matrix  $\gamma$  is symmetric for most common fibers.
- $\sum_{j=1}^3 \alpha_{ij} = 1$ ,  $\sum_{j=1}^3 \gamma_{ij} = 1$ ,  $\sum_{i=1}^3 \beta_{ij} = 1$ .
- Mode coupling at MUX/DEMUX is discrete in time. This discrete coupling generates mode peaks, represented by triangles in the Fig. 10. Different mode peaks result only from discrete coupling and are separated in time due to different mode group velocities in fiber. On the other hand, distributed coupling in fiber generates crosstalk plateau, represented by rectangular blocks in Fig. 10.
- For high performance mode-selective MUX/DEMUX (as those used in our experiment), the diagonal values in matrix  $\alpha$  and  $\beta$  are much larger than off-diagonal values. This is useful to simplify data processing.



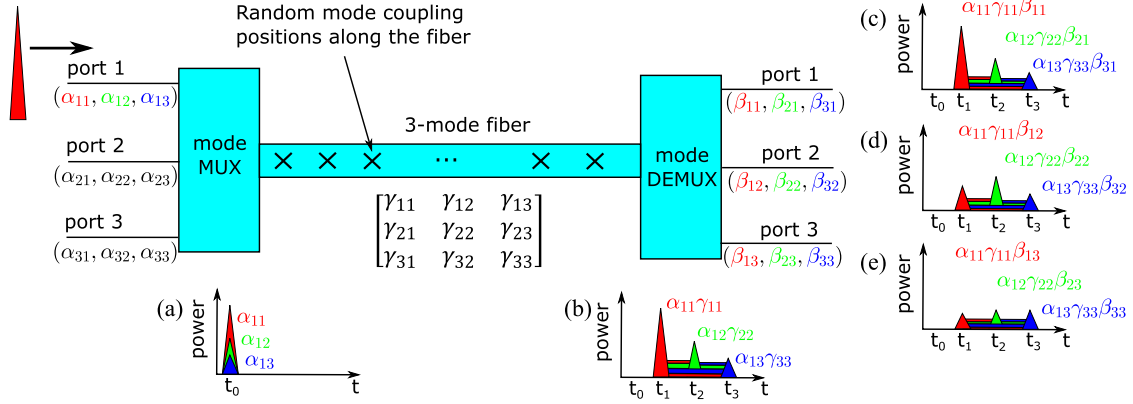


Fig. 10. 3-mode example with distributed coupling in the MMF: Launch unit pulse into one input port of multiplexer, and analyze impulse responses at all output ports of the demultiplexer.

The assumptions used in the 3-mode coupling analysis are as follows:

- Distributed mode coupling randomly occurs along the fiber, so the crosstalk plateau is uniformly distributed.
- The fiber is in “weak coupling regime”, not “strong coupling regime” [28]. So that in matrix  $\gamma$ , diagonal elements are much larger than off-diagonal elements.
- We don’t consider coupling back and forth in this simple model, e.g., mode G1 couples to G2 at some location then couples back to G1 somewhere later. We assume it only couples once throughout the fiber.
- We ignore loss and chromatic dispersion of the fiber.

We inject a pulse with unit energy into port 1 of MUX and analyze the impulse response at different locations of the system. Right after the mode MUX, three pulses are generated at time  $t_0$  with energy  $\alpha_{11}, \alpha_{12}, \alpha_{13}$ , as shown in inset (A) in Fig. 10 due to crosstalk (discrete coupling) of the MUX.

At the end of the 3-mode fiber, but right before the mode DEMUX, the impulse response is shown in inset (B). Mode peaks are separated due to DMDG. Letters labeled above each peak indicate how much energy remains in that mode peak (not in crosstalk plateau). The crosstalk plateau due to random coupling is represented by colored rectangular blocks between peaks. Taking the green rectangular block between  $t_1$  and  $t_2$  for example, it represents energy coupled from mode G1 to mode G2 after propagating through the fiber, with energy of  $\alpha_{11}\gamma_{12}$ . The physical meaning of this rectangular block should be interpreted as this: The left end of the green block at  $t_1$  represents the extreme case that mode G1 couples to G2 at the very end of the fiber, so that it takes minimum time to travel as it mostly propagates as mode G1 ( $v_1 > v_2$ ). The right end of the green block at  $t_2$  represents another extreme case that mode G1 couples to G2 at the very beginning of the fiber, so that it takes maximum time to travel as it mostly propagates as mode G2. The total energy in the plateau is given by summation of all six rectangular blocks:  $\alpha_{11}\gamma_{12} + \alpha_{11}\gamma_{13} + \alpha_{12}\gamma_{21} + \alpha_{12}\gamma_{23} + \alpha_{13}\gamma_{31} + \alpha_{13}\gamma_{32}$ .

After the mode DEMUX, the impulse response after each port is shown in (C), (D) and (E), respectively. Again, letters labeled above each peak indicate how much energy remains in that mode peak. We keep tracking of the energy left in the green

rectangular block between  $t_1$  and  $t_2$  and find it now has energy of  $\alpha_{11}\gamma_{12}\beta_{21}$ . The total energy in crosstalk plateau after port 1 is given by  $\alpha_{11}\gamma_{12}\beta_{21} + \alpha_{11}\gamma_{13}\beta_{31} + \alpha_{12}\gamma_{21}\beta_{11} + \alpha_{12}\gamma_{23}\beta_{31} + \alpha_{13}\gamma_{31}\beta_{11} + \alpha_{13}\gamma_{32}\beta_{21}$ .

If we inject unit pulse into all ports of the MUX, at the output of DEMUX, the complete  $3 \times 3$  matrix of energy in crosstalk plateau is given by the matrix product below, with plateau energy in (C), (D) and (E) the first row of the final matrix.

$$\begin{bmatrix} \alpha_{11} & \alpha_{12} & \alpha_{13} \\ \alpha_{21} & \alpha_{22} & \alpha_{23} \\ \alpha_{31} & \alpha_{32} & \alpha_{33} \end{bmatrix} \begin{bmatrix} 0 & \gamma_{12} & \gamma_{13} \\ \gamma_{21} & 0 & \gamma_{23} \\ \gamma_{31} & \gamma_{32} & 0 \end{bmatrix} \begin{bmatrix} \beta_{11} & \beta_{12} & \beta_{13} \\ \beta_{21} & \beta_{22} & \beta_{23} \\ \beta_{31} & \beta_{32} & \beta_{33} \end{bmatrix} \quad (4)$$

If we denote element (port 1, port 2) as “input from port 1 of MUX and output from port 2 of DEMUX,” then (port 1, port 2) of (4) is

$$\alpha_{11}\gamma_{12}\beta_{22} + \alpha_{11}\gamma_{13}\beta_{32} + \alpha_{12}\gamma_{21}\beta_{12} + \alpha_{12}\gamma_{23}\beta_{32} + \alpha_{13}\gamma_{31}\beta_{12} + \alpha_{13}\gamma_{32}\beta_{22} \quad (5)$$

In our calculation of Fig. 8 however, we didn’t count all crosstalk plateau values as that in (1) for simplification. Taking the “G1-G2” cell in Fig. 5 for example, we only integrated plateau energy between  $t_1$  and  $t_2$ . Using our method, (1) needs to be adapted to

$$\alpha_{11}\gamma_{12}\beta_{22} + \alpha_{12}\gamma_{21}\beta_{12} + \frac{t_2 - t_1}{t_3 - t_1}(\alpha_{13}\gamma_{31}\beta_{12} + \alpha_{11}\gamma_{13}\beta_{32}) \quad (6)$$

Although (1) is smaller than (1), their values are close because two reasons below are satisfied in our experiment:

- For high performance mode-selective MUX/DEMUX made of MPLC, the diagonal values in matrix  $\alpha$  and  $\beta$  are much larger than off-diagonal values.
- For fibers in “weak coupling regime” with coupling matrix  $\gamma$ , diagonal elements are much larger than off-diagonal elements.

This justifies our normalization method in Fig. 8. Our method is simple without losing its accuracy. Above analysis shows that matrix  $\gamma$  contains exact information that reflects the true

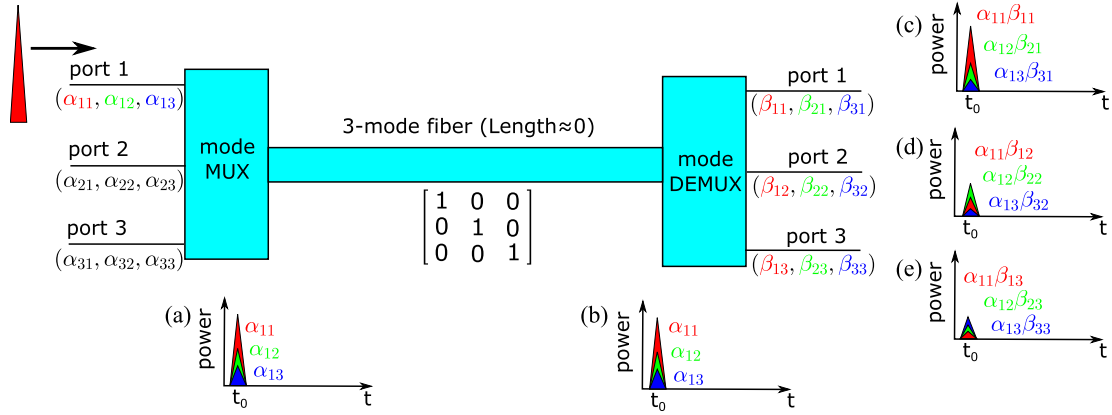


Fig. 11. 3-mode example of back-to-back propagation: Launch unit pulse into one input port of multiplexer, and analyze impulse responses at all output ports of the demultiplexer.

crosstalk plateau level for any mode pair of the MMF. However, (1) shows that the measured crosstalk plateau of the impulse response is “polluted” by the crosstalk of MUX and DEMUX. Matrix  $\gamma$  cannot be recovered without complete knowledge of the crosstalk of mode MUX/DEMUX. With an ideal MUX/DEMUX, the final matrix that describes the total energy in crosstalk plateau is given by

$$\begin{bmatrix} 1 & 0 & 0 \\ 0 & 1 & 0 \\ 0 & 0 & 1 \end{bmatrix} \begin{bmatrix} 0 & \gamma_{12} & \gamma_{13} \\ \gamma_{21} & 0 & \gamma_{23} \\ \gamma_{31} & \gamma_{32} & 0 \end{bmatrix} \begin{bmatrix} 1 & 0 & 0 \\ 0 & 1 & 0 \\ 0 & 0 & 1 \end{bmatrix} \quad (7)$$

Compare the measured plateau value ((1) or (1)) with the true value  $\gamma_{12}$ , it’s hard to tell whether the measured value is larger or smaller than the true value. It really depends on the MUX/DEMUX and fiber used in the measurement considering that  $0 \leq \alpha_{ij}, \beta_{ij}, \gamma_{ij} \leq 1$ .

For BTB in Fig. 9(a), matrix  $\gamma$  can be regarded as an identity matrix, as shown in Fig. 11. For this 3-mode model we have

$$\begin{bmatrix} \alpha_{11} & \alpha_{12} & \alpha_{13} \\ \alpha_{21} & \alpha_{22} & \alpha_{23} \\ \alpha_{31} & \alpha_{32} & \alpha_{33} \end{bmatrix} \begin{bmatrix} 1 & 0 & 0 \\ 0 & 1 & 0 \\ 0 & 0 & 1 \end{bmatrix} \begin{bmatrix} \beta_{11} & \beta_{12} & \beta_{13} \\ \beta_{21} & \beta_{22} & \beta_{23} \\ \beta_{31} & \beta_{32} & \beta_{33} \end{bmatrix} = \alpha\beta \quad (8)$$

For Fig. 9(b) that gives the total coupling results including the MUX/DEMUX and fiber, we can also use the 3-mode coupling example to explain. In this case total energy of the impulse response, including the mode peaks and crosstalk plateau is given by:

$$\begin{bmatrix} \alpha_{11} & \alpha_{12} & \alpha_{13} \\ \alpha_{21} & \alpha_{22} & \alpha_{23} \\ \alpha_{31} & \alpha_{32} & \alpha_{33} \end{bmatrix} \begin{bmatrix} \gamma_{11} & \gamma_{12} & \gamma_{13} \\ \gamma_{21} & \gamma_{22} & \gamma_{23} \\ \gamma_{31} & \gamma_{32} & \gamma_{33} \end{bmatrix} \begin{bmatrix} \beta_{11} & \beta_{12} & \beta_{13} \\ \beta_{21} & \beta_{22} & \beta_{23} \\ \beta_{31} & \beta_{32} & \beta_{33} \end{bmatrix} = \alpha\gamma\beta \quad (9)$$

It’s clear that without complete knowledge of  $\alpha$  and  $\beta$ , but simply knowing the product of  $\alpha\beta$  and  $\alpha\gamma\beta$ , we cannot solve for  $\gamma$ .

## V. CONCLUSION

In conclusion, SNSPDs offer unprecedented opportunity to study weak modal interactions in multimode optical fibers. Using SNSPD and two 45-mode MPLCs, we measure the mode transfer matrix of a commercial OM3 multimode fiber with the time-of-flight method. High sensitivity ( $-136$  dBm) and high timing accuracy ( $\sim 10$  ps) give us unprecedented capability to accurately measure very weak modal dynamics, including distributed mode coupling, differential mode group delay, and cladding modes of multimode fibers. These remarkable capability for accurate characterization of light-scrambling in multimode fiber could prove useful for a variety of applications such as key exchange in quantum key distribution schemes over commercial multimode fibers [29].

## ACKNOWLEDGMENT

Y. Zhang thanks Pouria Sanjari (University of Pennsylvania, Nokia Bell Labs summer intern 2021) for help on the measurement of timing jitter of quTAG, and thanks Rene-Jean Essiambre (Nokia Bell Labs) for thoughtful discussions on the measured pedestal floor.

## VI. SUPPLEMENTARY

We provide large figures of the entire  $45 \times 45$  mode transfer matrix of the BTB ( $3 \sim 43$  ns) and MMF ( $677 \sim 717$  ns) measurement in the **supplementary**. For BTB the 2nd peak appearing at about 33 ns, corresponding to a round trip fiber delay of 1.5 m, was due to reflections from the experimental setup [19]. As in the BTB case, in MMF the 2nd peak at 706 ns is also due to reflections in the system.

## REFERENCES

- [1] P. J. Winzer, D. T. Neilson, and A. R. Chraplyvy, “Fiber-optic transmission and networking: The previous 20 and the next 20 years,” *Opt. Exp.*, vol. 26, no. 18, pp. 24190–24239, 2018.
- [2] G. Li, N. Bai, N. Zhao, and C. Xia, “Space-division multiplexing: The next frontier in optical communication,” *Adv. Opt. Photon.*, vol. 6, no. 4, pp. 413–487, 2014.
- [3] S. Ö. Arik, D. Askarov, and J. M. Kahn, “Effect of mode coupling on signal processing complexity in mode-division multiplexing,” *J. Lightw. Technol.*, vol. 31, no. 3, pp. 423–431, Feb. 2013.

- [4] Y. Painchaud, P. LeBel, M. Duguay, and R. J. Black, "Time-resolved identification of modes and measurement of intermodal dispersion in optical fibers," *Appl. Opt.*, vol. 31, no. 12, pp. 2005–2010, 1992.
- [5] J. Cheng, M. E. Pedersen, K. Wang, C. Xu, L. Grüner-Nielsen, and D. Jakobsen, "Time-domain multimode dispersion measurement in a higher-order-mode fiber," *Opt. Lett.*, vol. 37, no. 3, pp. 347–349, 2012.
- [6] G. D. VanWiggeren and D. M. Baney, "Swept-wavelength interferometric analysis of multiport components," *IEEE Photon. Technol. Lett.*, vol. 15, no. 9, pp. 1267–1269, Sep. 2003.
- [7] M. Nakazawa, M. Yoshida, and T. Hirooka, "Measurement of mode coupling distribution along a few-mode fiber using a synchronous multi-channel OTDR," *Opt. Exp.*, vol. 22, no. 25, pp. 31 299–31 309, 2014.
- [8] R. Ryf, R.-J. Essiambre, S. Randel, M. Mestre, C. Schmidt, and P. Winzer, "Impulse response analysis of coupled-core 3-core fibers," in *Proc. 38th Eur. Conf. Exhib. Opt. Commun.*, 2012, pp. 1–3.
- [9] S. Gyger *et al.*, "Reconfigurable photonics with on-chip single-photon detectors," *Nature Commun.*, vol. 12, no. 1, pp. 1–8, 2021.
- [10] M. Shangguan *et al.*, "Dual-frequency Doppler lidar for wind detection with a superconducting nanowire single-photon detector," *Opt. Lett.*, vol. 42, no. 18, pp. 3541–3544, 2017.
- [11] R. H. Hadfield, "Single-photon detectors for optical quantum information applications," *Nature Photon.*, vol. 3, no. 12, pp. 696–705, 2009.
- [12] H.-S. Zhong *et al.*, "Quantum computational advantage using photons," *Science*, vol. 370, no. 6523, pp. 1460–1463, 2020.
- [13] H.-S. Zhong *et al.*, "Phase-programmable Gaussian boson sampling using stimulated squeezed light," *Phys. Rev. Lett.*, vol. 127, no. 18, 2021, Art. no. 180502.
- [14] H. Takesue *et al.*, "Quantum key distribution over a 40-dB channel loss using superconducting single-photon detectors," *Nature Photon.*, vol. 1, no. 6, pp. 343–348, 2007.
- [15] S. D. Johnson, D. B. Phillips, Z. Ma, S. Ramachandran, and M. J. Padgett, "A light-in-flight single-pixel camera for use in the visible and short-wave infrared," *Opt. Exp.*, vol. 27, no. 7, pp. 9829–9837, 2019.
- [16] H. K. Chandrasekharan *et al.*, "Observing mode-dependent wavelength-to-time mapping in few-mode fibers using a single-photon detector array," *APL Photon.*, vol. 5, no. 6, 2020, Art. no. 061303.
- [17] IDQ, Id230 infrared single-photon detector. [Online]. Available: <https://www.idquantique.com/quantum-sensing/products/id230/>
- [18] B. Korzh *et al.*, "Demonstration of sub-3 ps temporal resolution with a superconducting nanowire single-photon detector," *Nature Photon.*, vol. 14, no. 4, pp. 250–255, 2020.
- [19] M. Mazur, N. K. Fontaine, R. Ryf, H. Chen, and A. Blanco-Redondo, "Impulse response measurement of a few-mode fiber using superconductive nanowire single-photon detectors," in *Proc. Eur. Conf. Opt. Commun.*, 2021, pp. 1–4.
- [20] Single-Quantum. Operation principle of SNSPD. [Online]. Available: <https://singlequantum.com/technology/snsdp/>
- [21] N. K. Fontaine *et al.*, "Packaged 45-mode multiplexers for a 50- $\mu\text{m}$  graded index fiber," in *Proc. Eur. Conf. Opt. Commun.*, 2018, pp. 1–3.
- [22] H. Shibata, K. Shimizu, H. Takesue, and Y. Tokura, "Ultimate low system dark-count rate for superconducting nanowire single-photon detector," *Opt. Lett.*, vol. 40, no. 14, pp. 3428–3431, 2015.
- [23] R. Ryf *et al.*, "Mode-multiplexed transmission over conventional graded-index multimode fibers," *Opt. Exp.*, vol. 23, no. 1, pp. 235–246, 2015.
- [24] N. K. Fontaine, R. Ryf, H. Chen, D. Neilson, and J. Carpenter, "Design of high order mode-multiplexers using multiplane light conversion," in *Proc. Eur. Conf. Opt. Commun.*, 2017, pp. 1–3.
- [25] O. V. Ivanov, S. A. Nikitov, and Y. V. Gulyaev, "Cladding modes of optical fibers: Properties and applications," *Phys.-Uspekhi*, vol. 49, no. 2, 2006, Art. no. 167.
- [26] N. K. Fontaine *et al.*, "Characterization of space-division multiplexing systems using a swept-wavelength interferometer," in *Proc. Opt. Fiber Commun. Conf.*, 2013, pp. 1–3.
- [27] J. Zhang *et al.*, "Accurate mode-coupling characterization of low-crosstalk ring-core fibers using integral calculation based swept-wavelength interferometry measurement," *J. Lightw. Technol.*, vol. 39, no. 20, pp. 6479–6486, Oct. 2021.
- [28] D. M. Marom, R. Ryf, and D. T. Neilson, "Networking and routing in space-division multiplexed systems," in *Optical Fiber Telecommunications VII*. Amsterdam, The Netherlands: Elsevier, 2020, pp. 719–750.
- [29] L. V. Amitonova, T. B. Tentrup, I. M. Vellekoop, and P. W. Pinkse, "Quantum key establishment via a multimode fiber," *Opt. Exp.*, vol. 28, no. 5, pp. 5965–5981, 2020.